

***s*-wave average neutron resonance parameters of  $^{175}\text{Lu} + n$** 


G. Noguere and O. Bouland

*CEA, DEN Cadarache, F-13108 Saint Paul Les Durance, France*

J. Heyse, S. Kopecky, C. Paradela, and P. Schillebeeckx

*EC-JRC-IRMM, B-2440 Geel, Belgium*

A. Ebran and O. Roig

*CEA, DAM, DIF, F-91297 Arpajon, France* (Received 1 April 2019; revised manuscript received 28 October 2019; published 30 December 2019)

Resonance energies  $E_\lambda$ , neutron widths  $\Gamma_{n,\lambda}$ , and radiation widths  $\Gamma_{\gamma,\lambda}$  for the compound system  $^{175}\text{Lu} + n$  were determined up to 1 keV from time-of-flight data reported in literature and recently measured at the GELINA facility of JRC-Geel (Belgium). The statistical analysis of the obtained resonance parameters provides an *s*-wave neutron strength function [ $S_0 = 1.96(8)$ ], mean level spacing [ $D_0 = 3.24(9)$  eV], and average radiation width ( $\langle\Gamma_{\gamma_0}\rangle = 61.3(59)$  meV) which are substantially different from those compiled in libraries dedicated to statistical calculations. The largest difference lies on the average radiation width, for which a value of 77(5) meV is recommended.  $^{175}\text{Lu}$  neutron cross sections were calculated with the TALYS code by using our *s*-wave average parameters as constraints. At  $kT = 30$  keV, we obtain a total neutron capture cross section equal to 1125(62) mbarns, confirming the lower values reported in the 1990s.

DOI: [10.1103/PhysRevC.100.065806](https://doi.org/10.1103/PhysRevC.100.065806)**I. INTRODUCTION**

In neutron resonance spectroscopy, average neutron resonance parameters are neutron strength functions, average radiation widths, and mean level spacings between resonances. Each parameter is given at  $S_n$ . These parameters are of great interest for testing nuclear structure models. They are also important parameters for various nuclear applications such as for calculation of reaction cross sections applied to astrophysical nucleosynthesis in the keV neutron energy range. In the mass region of the rare earth elements, the neutron capture cross sections of  $^{175}\text{Lu}$  to the  $^{176}\text{Lu}$  ground and isomeric states play a role in the *s*-process reaction path from  $^{168}\text{Er}$  to  $^{178}\text{Hf}$  in which a branch point exists for lutetium [1].

Values of average neutron resonance parameters are suggested by the Reference Input Parameter Library (RIPL) [2–4] and the Atlas of Neutron Resonances (ANR) [5]. They are given as a function of the orbital angular momentum  $l$  of the incoming neutron. Table I compares the *s*-wave ( $l = 0$ ) average resonance parameters compiled in RIPL and ANR. Values adopted in the first two versions of the RIPL library (RIPL-1 and RIPL-2) were suggested by Ignatyuk [6]. In RIPL-1, the erroneous value of the mean level spacing ( $D_0 = 6.05$  eV) has been corrected in RIPL-2 and a value of 3 eV, in better agreement with the mean level spacing compiled in the Atlas of Neutron Resonances, was adopted. Latest recommended values come from the experimental work of Liou *et al.* [7], in which  $D_0 = 3.45(15)$  meV,  $10^4 S_0 = 1.83(12)$ , and  $\langle\Gamma_{\gamma_0}\rangle = 77$  meV. These results were established by a statistical analysis of the resonance parameters extracted from

high-resolution transmission measurements carried out at the Columbia University Nevis synchrocyclotron. In their work, Liou *et al.* only provide the range of variation of the individual radiation widths from 59(20) to 100(20) meV for 40 levels. Such a large spread between the radiation widths makes questionable the small uncertainty of  $\pm 5$  meV quoted in Table I. This doubtful result can have sizable impact on the calculation of the  $^{175}\text{Lu}$  capture cross section in the continuum energy range, above the upper energy limit of the resolved resonance range. The goal of the present work is to calculate the total capture cross section of  $^{175}\text{Lu}$  to the  $^{176}\text{Lu}$  ground and isomeric states thanks to *s*-wave average neutron resonance parameters extracted from capture and transmission data measured by the time-of-flight technique.

Lutetium isotopes were the subject of recent time-of-flight experiments performed by the CEA/DAM of Bruyere le Châtel at the Los Alamos National Laboratory using the DANCE array [8–13]. Neutron capture measurements on  $^{173}\text{Lu}$ ,  $^{175}\text{Lu}$ , and  $^{176}\text{Lu}$  have been undertaken using isotopically enriched targets and natural lutetium samples. Complementary transmission measurements on natural samples were carried out at the GELINA facility of the Joint Research Center of Geel (JRC-Geel) with the aim of improving the  $^{175}\text{Lu}$  resonance parameters up to 1 keV.

Previous experimental works of interest for the present study are presented in Sec. II. Section III provides resonance energies  $E_\lambda$ , radiation widths  $\Gamma_{\lambda,\gamma}$ , and neutron widths  $\Gamma_{\lambda,n}$  of resonances  $\lambda$  assessed with the shape analysis code REFIT [14] using the Reich-Moore approximation [15] of the *R*-matrix theory [16]. Time-of-flight data measured at the GELINA

TABLE I. Mean level spacing  $D_0$  (in meV), neutron strength function  $S_0$ , and average radiation width ( $\Gamma_{\gamma_0}$ ) (in meV) for the compound system  $^{175}\text{Lu} + n$  as compiled in the Reference Input Parameter Library (RIPL) and in the Atlas of Neutron Resonances (ANR).

Library	Year	Ref.	$D_0$	$10^4 S_0$	$(\Gamma_{\gamma_0})$
RIPL-1	1998	[2]	6.05(15)	1.78(12)	77(23)
RIPL-2	2006	[3]	3.0(4)	1.8(3)	77(23)
RIPL-3	2009	[4]	3.45(15)	1.82(12)	77(5)
ANR	2006	[5]	3.45(15)	1.82(12)	77(5)

facility were analyzed simultaneously with data retrieved from the experimental database EXFOR [17]. Average neutron resonance parameters are given in Sec. IV. They have been deduced from the obtained resonance parameters with a statistical method relying on the Porter-Thomas distribution of the reduced neutron widths [18], which accounts for missing levels. In Sec. V, the resulting  $s$ -wave neutron strength function, mean level spacing, and average radiation width were used to optimize optical and statistical model parameters. Average total and capture cross sections were calculated above 1 keV with the TALYS code [19]. Agreements between our theoretical calculations and data reported in the literature are discussed with special attention to the  $^{175}\text{Lu}$  capture cross section at  $kT = 30$  keV.

## II. REVIEW OF CAPTURE AND TRANSMISSION DATA

The data sets of interest for this work were retrieved from the experimental database EXFOR [17], in which are given full experimental information and related references. Table II reports the data sets used for the resonance analysis and Table III lists the average capture and total cross sections that will be compared in Sec. V with our optical and statistical model calculations.

The  $^{175}\text{Lu}$  resonance parameters were determined from time-of-flight data measured with isotopically enriched and natural samples. Although the natural abundance of  $^{176}\text{Lu}$  is

TABLE III.  $^{175}\text{Lu}$  average capture and total cross sections used in the present work above 3 keV. The total cross section from Liou *et al.* is derived from the transmission data listed in Table II measured with the thick sample.

Author	Year	Ref.	Cross section type	Energy range
Liou	1975	[7]	Total	$E < 3$ keV
Wisshak	2006	[20]	total	$10 < E < 200$ keV
Macklin	1978	[21]	Capture	$3 < E < 1900$ keV
Beer	1984	[22]	Capture	$10 < E < 200$ keV
Wisshak	2006	[20]	Capture	$3 < E < 225$ keV

rather low (2.6%) compared to  $^{175}\text{Lu}$  (97.4%), its contribution in data measured with natural samples is not negligible and  $^{176}\text{Lu}$  can create complex overlapping structures with  $^{175}\text{Lu}$ . Consequently, we have included in the analysis total and capture cross sections data measured with enriched  $^{176}\text{Lu}$  targets. Most of the data sets listed in Table II were used for studying the low neutron energy range below 3.5 eV with the aim of verifying parameters of the first  $^{176}\text{Lu}$  and  $^{175}\text{Lu}$  resonances at 0.143 and 2.606 eV, respectively. Only works of Liou *et al.* [7] and Roig *et al.* [12] were used over a wider energy range, reaching up to 1.0 keV for  $^{175}\text{Lu}$  and 400 eV for  $^{176}\text{Lu}$ . The capture yield measured by Roig *et al.* with an enriched  $^{175}\text{Lu}$  sample is also part of the experimental program on lutetium isotopes carried out by CEA/DAM at Los Alamos National Laboratory using the DANCE array. The experimental conditions are similar to those used for measuring the  $^{176}\text{Lu}$  capture cross section. In the present work, we have used the transmission data of Liou *et al.* measured with a thin sample between 18 and 44 eV. The second transmission data set measured with a thick sample was used from 55 eV.

Above the resolved resonance range, only a few  $^{175}\text{Lu}$  average capture and total cross sections are tabulated in EXFOR. In Table III, we have recovered the total cross section from Liou *et al.* from the transmission data of Table II measured with the thick sample. This data set was converted in total

TABLE II. List of data sets retrieved from the experimental database EXFOR [17] and used in the present work for determining  $^{175}\text{Lu}$  and  $^{176}\text{Lu}$  neutron resonance parameters, up to 1 keV and 400 eV, respectively.

Sample	Author	Year	Data type	Flight length	Energy range
$^{nat}\text{Lu}$	Brunner	1967	Transmission	15 m	$E < 3.5$ eV
$^{nat}\text{Lu}$	Zimmerman	1967	Transmission		$E < 1.3$ eV
$^{nat}\text{Lu}$	Young	1968	Transmission		$E < 0.3$ eV
$^{nat}\text{Lu}$	Widder	1975	Capture yield		$E < 2.0$ eV
$^{176}\text{Lu}$	Baston	1960	Transmission	11 m	$E < 0.3$ eV
$^{176}\text{Lu}$	Roberge	1960	Transmission		$E < 0.3$ eV
$^{176}\text{Lu}$	Young	1968	Transmission		$E < 0.3$ eV
$^{176}\text{Lu}$	Roig	2016	Capture yield	20.25 m	$1.0 < E < 400$ eV
$^{175}\text{Lu}$	Widder	1975	Capture yield		$E < 2.0$ eV
$^{175}\text{Lu}$	Liou	1975	Transmission (thin sample)	39.57 m	$18.0 < E < 44.0$ eV
$^{175}\text{Lu}$	Liou	1975	Transmission (thick sample)	202.05 m	$55.0 < E < 1000.0$ eV
$^{175}\text{Lu}$	Roig	2013	Capture yield	20.25 m	$8.5 < E < 44.0$ eV

TABLE IV. New transmission data measured at the GELINA facility at a flight length  $L = 10.861(2)$  m with natural lutetium samples. The thick sample of 2 mm is a stack of two thin samples of 1 mm each.

Sample thickness	Sample stack	Sample geometry	Areal density	Antioverlap and black resonance filters	Energy range
2 mm	1st+2nd	$2.5 \times 2.5$ cm	$6.8(2) \times 10^{-3}$ at/b	B,Co,Na	$1.0 < E < 1000.0$ eV
2 mm	1st+2nd	$2.5 \times 2.5$ cm	$6.8(2) \times 10^{-3}$ at/b	Cd,Co,Na	$1.0 < E < 105.0$ eV
1 mm	1st	$2.5 \times 2.5$ cm	$3.4(1) \times 10^{-3}$ at/b	B,Co,Na	$1.0 < E < 250.0$ eV
1 mm	1st	$2.5 \times 2.5$ cm	$3.4(1) \times 10^{-3}$ at/b	Cd,Co,Na	$1.0 < E < 105.0$ eV
1 mm	1st	$2.5 \times 2.5$ cm	$3.4(1) \times 10^{-3}$ at/b	B,Na	$1.0 < E < 250.0$ eV
1 mm	1st	$2.5 \times 2.5$ cm	$3.4(1) \times 10^{-3}$ at/b	Cd,Na	$1.0 < E < 105.0$ eV
1 mm	2nd	$2.5 \times 2.5$ cm	$3.4(1) \times 10^{-3}$ at/b	B,Co,Na	$1.0 < E < 250.0$ eV
0.15 mm		$2.5 \times 2.5$ cm	$5.1(10) \times 10^{-4}$ at/b	B,Co,Na	$1.0 < E < 55.0$ eV
0.15 mm		$2.5 \times 2.5$ cm	$5.1(10) \times 10^{-4}$ at/b	B,Co,Na	$1.0 < E < 55.0$ eV

cross section, averaged over a broad energy mesh, and corrected for resonance self-shielding effect.

### III. NEUTRON RESONANCE SPECTROSCOPY

Neutron resonance spectroscopy on  $^{175}\text{Lu}$  consists of determining energy and partial reaction widths of each resonance by using the neutron resonance shape analysis technique in association with the Reich-Moore approximation of the  $R$ -matrix theory. The analysis was performed with the REFIT code. New data sets used in the present work and principles of the analysis are briefly described in this section.

#### A. Transmission data measured at GELINA

For lutetium, transmission measurements in Table IV were performed at a flight station at  $L = 10.861(2)$  m in the GELINA facility [23]. The GELINA facility is based on an electron accelerator providing a pulse white neutron source. The accelerator was operated with a frequency of 800 Hz. At the exit of the accelerator, a compression magnet provides an electron burst with a width less than 2 ns. Neutrons are produced by Bremsstrahlung radiation via the slowing of electrons in a water-moderated uranium target. Neutrons emitted from the target-moderator assembly are directed to the measurement stations through evacuated aluminium pipes. In the case of the transmission experiments investigated in this work, neutrons were detected by Li-glass detectors. Neutron spectroscopy experiments carried out at the GELINA facility are based on the time-of-flight technique that consists of connecting the neutron energies  $E$  to their flight times  $t$ , given the flight length  $L$  between the neutron source and the detectors. The present experiments were performed during the same period as natural silver samples. Results for silver are reported in Ref. [24] together with a detailed description of the detection setup and explanations of the experimental corrections.

Experimental details on the transmission experiments carried out at the GELINA facility with natural lutetium samples are summarized in Table IV. Three sample thicknesses (2, 1, and 0.15 mm) were measured with different antioverlap

and black resonance filter configurations. The thick sample is a stack of two metallic lutetium samples of 1 mm each. These two thin samples were measured separately in order to cross-check the consistency of the areal density of  $3.4 \times 10^{-3}$  atom/barn and the tantalum impurity. The very thin sample of 0.15 mm was useful for improving the  $^{175}\text{Lu}$  resonance doublet around 13.9 and 14.1 eV.

Experimental transmission  $\mathcal{T}_{\text{exp}}$  of a given homogeneous sample perpendicular to the incident neutron beam is defined as the ratio of the transmitted neutron flux to the incident neutron flux. Both neutron fluxes are measured sequentially in a two-step sequence, namely sample *in* (the beam) and sample *out* (of the beam) positions. The final transmission can then be expressed as a function of the time-of-flight  $t$ :

$$\mathcal{T}_{\text{exp}}(t) = N_{\mathcal{T}} \frac{C_{\text{in}}(t) - KB_{\text{in}}(t)}{C_{\text{out}}(t) - KB_{\text{out}}(t)}, \quad (1)$$

in which  $C(t)$  stands for the number of neutrons detected by a Li-glass detector corrected for dead time and normalized by the same time-bin width structure and the neutron beam intensity. The neutron beam intensity is constantly monitored with boron detectors located in the roof above the GELINA neutron target.  $B(t)$  is the background contribution determined via the black resonance technique. Constant terms and exponential functions were combined to reproduce the shape of the background, whose parameters were adjusted on the bottom of black resonances using dedicated experimental runs carried out with a full set of black resonance filters. For the lutetium measurements, Co (132 eV) and Na (2.8 keV) black resonance filters were used to scale the background level of each time spectrum. In the cases of the thick (2 mm) and intermediate (1 mm) samples, few  $^{175}\text{Lu}$  black resonances were also used to fit the background shape below 20 eV. The factor  $K = 1.00(3)$  in Eq. (1) was introduced to account for systematic uncertainties due to the background model.  $N_{\mathcal{T}}$  is a normalization factor introduced to account for the uncertainty on the neutron beam intensity measured by the flux monitors. Uncertainty on  $N_{\mathcal{T}}$  is lower than 0.25%. All data reduction steps are conveniently handled by the AGS code [25]. The final experimental uncertainty  $u_{\mathcal{T}_{\text{exp}}}$  accounts for both correlated and uncorrelated uncertainties. Examples of transmission data measured up to 79 eV are shown in

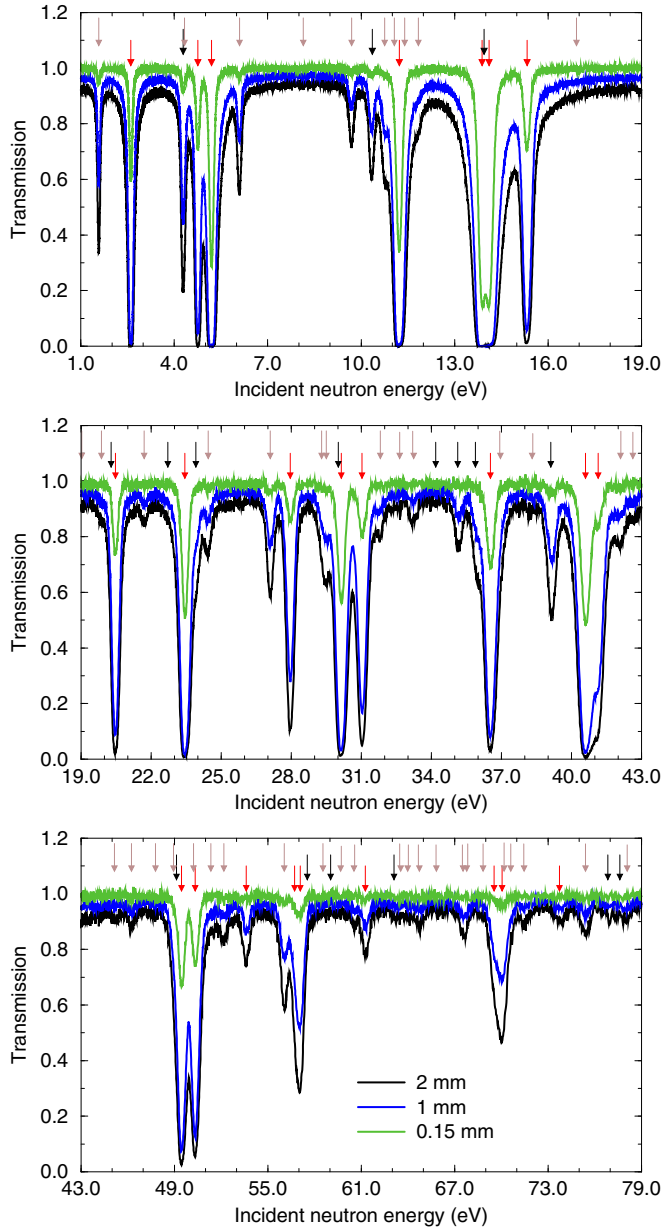


FIG. 1. Examples of transmission data measured at the GELINA facility up to 79 eV with natural lutetium samples of thicknesses equal to 2 mm (black line), 1 mm (blue line), and 0.15 mm (green line). Red, brown, and black arrows indicate the energies of the  $^{175}\text{Lu}$ ,  $^{176}\text{Lu}$ , and  $^{181}\text{Ta}$  resonances, respectively.

Fig. 1. Arrows indicate energies of the  $^{175}\text{Lu}$ ,  $^{176}\text{Lu}$ , and  $^{181}\text{Ta}$  resonances. Isotopic contributions of  $^{176}\text{Lu}$  and  $^{181}\text{Ta}$  are not removed from the data. They are included in the neutron resonance shape analysis procedure. The impact of the  $^{181}\text{Ta}$  resonances on the final results is discussed in Sec. III C.

### B. Neutron resonance shape analysis

In the resolved resonance range of neutron cross sections, the analysis of time-of-flight data mainly consists of extract-

ing energies and partial reaction widths of observed resonances. For this purpose, the least-squares fitting code REFIT [14] is routinely used at JRC-Geel to study data measured at the GELINA facility. Theoretical transmission is given by the expression

$$\mathcal{T}_{th}(t) = \int_0^{+\infty} R_T(t, E) \exp\left(\sum_i n_i \sigma_{\text{tot},i}(E)\right) dE, \quad (2)$$

and capture yield for thin sample can be conveniently defined as follows:

$$\mathcal{Y}_{th}(t) \simeq \int_0^{+\infty} R_Y(t, E) [1 - \mathcal{T}_{th}(E)] \frac{\sum_i \varepsilon_i n_i \sigma_{\gamma,i}(E)}{\sum_i n_i \sigma_{\text{tot},i}(E)} dE. \quad (3)$$

For representation purposes, time-dependent variables have been translated into energy by supposing a constant flight path length. In these two equations,  $\sigma_{\text{tot},i}$  and  $\sigma_{\gamma,i}$  are the total and capture cross sections of the nuclide  $i$ , which are Doppler broadened with the free gas model at an effective temperature  $T_{\text{eff}}$  [26]. The probability density functions  $R_T(t, E)$  and  $R_Y(t, E)$  stand for the experimental response functions of the facility that represent the distribution of neutron flight time, whose full width at half maximum mainly depends on the characteristics of the pulsed neutron source. A combination of a chi-squared function with six degrees of freedom with exponential tails is suitable to analytically describe the response function of most time-of-flight facilities up to 1 keV [27]. In Eq. (3), the variable  $\varepsilon_i$  is related to the detection efficiency of the  $\gamma$  rays emitted after neutron capture by the target isotope  $i$ . In the present work,  $\varepsilon$  was simply taken equal to unity because the  $^{175}\text{Lu}$  and  $^{176}\text{Lu}$  capture yields measured by Roig *et al.* (Table II) were obtained with very thin highly enriched samples (areal densities of the order of  $10^{-6}$  atom/barn). Therefore, the radiative capture efficiency was included in the normalization factor, which was determined using the first  $^{175}\text{Lu}$  and  $^{176}\text{Lu}$  resonances observed in the transmission data.

The isotopes included in the analysis are  $^{175}\text{Lu}$ ,  $^{176}\text{Lu}$ ,  $^{181}\text{Ta}$ , and  $^{16}\text{O}$ . The prior  $^{175}\text{Lu}$  resonance parameter values introduced in the fitting procedure were taken from the JEFF-3.1.1 data library [28], which is based on the parameters established by Liou *et al.* [7]. Those for  $^{176}\text{Lu}$  were taken from Ref. [12]. The  $^{181}\text{Ta}$  resonance parameters were those compiled in JEFF-3.1.1. In the low neutron energy range, the contribution of the  $^{16}\text{O}(n, \text{tot})$  cross section is constant and nearly equal to 3.8 barns [5].

Posterior values of the  $^{175}\text{Lu}$  resonance parameters are reported in Table V. They were obtained with the REFIT code from the simultaneous analysis of the capture and transmission data listed in Tables II and IV. As already stated by Liou *et al.*, the two possible statistical spin factors  $g_J$  (7/16 and 9/16) are nearly equal for  $^{175}\text{Lu}$  ( $J^\pi = 7/2^+$ ). Consequently, no attempt was made to change the spin of the resonances ( $J^\pi = 3^+, 4^+$ ) and they were all supposed to be  $s$ -wave resonances ( $l = 0$ ). An average radiation width of 61.3 meV was deduced from the total widths of 16 resonances below 50 eV. More explanations on the average radiation width and



TABLE V.  $^{175}\text{Lu}$  resonance parameters below 1 keV given by the REFIT code from the simultaneous analysis of the capture and transmission data listed in Tables II and IV. The average radiation width of 61.3(59) meV (identified with an asterisk) is imposed in the analysis when the total width of the studied resonance cannot be extracted from the data (see Sec. IV B).

$E_\lambda$ (eV)	$J^\pi$ ( $h^-$ )	$\Gamma_{\lambda\gamma}$ (meV)	$\Gamma_{\lambda n}$ (meV)
-17.650(0)	4 <sup>+</sup>	56.1(50)	98.3(59)
2.606(1)	4 <sup>+</sup>	59.4(10)	0.21(1)
4.759(3)	4 <sup>+</sup>	57.8(13)	0.30(1)
5.198(3)	3 <sup>+</sup>	63.4(20)	1.71(4)
11.225(6)	3 <sup>+</sup>	60.6(24)	4.29(13)
13.882(8)	4 <sup>+</sup>	57.2(21)	7.19(21)
14.110(8)	3 <sup>+</sup>	67.8(35)	10.86(33)
15.328(8)	4 <sup>+</sup>	58.4(41)	1.61(6)
20.478(11)	3 <sup>+</sup>	59.1(54)	2.82(13)
23.457(13)	3 <sup>+</sup>	63.8(55)	8.12(48)
27.967(15)	4 <sup>+</sup>	57.7(86)	1.72(7)
30.148(16)	4 <sup>+</sup>	63.5(72)	7.92(59)
31.042(17)	4 <sup>+</sup>	60.6(96)	3.03(15)
36.542(20)	3 <sup>+</sup>	60.0(105)	8.62(69)
40.613(22)	3 <sup>+</sup>	62.7(95)	22.1(12)
41.150(22)	4 <sup>+</sup>	61.3(59)*	3.09(18)
49.464(27)	3 <sup>+</sup>	69.4(150)	16.1(15)
50.336(27)	4 <sup>+</sup>	58.8(153)	9.16(87)
53.612(29)	4 <sup>+</sup>	61.3(59)*	0.38(2)
56.733(31)	3 <sup>+</sup>	61.3(59)*	1.15(9)
57.083(32)	3 <sup>+</sup>	61.3(59)*	3.27(22)
61.265(33)	4 <sup>+</sup>	61.3(59)*	0.42(2)
69.555(38)	4 <sup>+</sup>	61.3(59)*	1.05(4)
70.062(37)	3 <sup>+</sup>	61.3(59)*	2.56(11)
73.746(40)	3 <sup>+</sup>	61.3(59)*	0.21(4)
81.144(43)	3 <sup>+</sup>	61.3(59)*	0.30(3)
85.613(45)	4 <sup>+</sup>	61.3(59)*	8.49(51)
86.358(101)	3 <sup>+</sup>	61.3(59)*	0.11(4)
88.224(49)	3 <sup>+</sup>	61.3(59)*	1.35(10)
88.682(49)	3 <sup>+</sup>	61.3(59)*	3.94(25)
96.854(51)	4 <sup>+</sup>	61.3(59)*	79.5(28)
98.475(101)	3 <sup>+</sup>	61.3(59)*	0.11(2)
99.897(56)	3 <sup>+</sup>	61.3(59)*	14.13(71)
101.000(54)	4 <sup>+</sup>	61.3(59)*	6.53(29)
103.130(55)	4 <sup>+</sup>	61.3(59)*	10.38(61)
107.590(57)	4 <sup>+</sup>	61.3(59)*	35.9(25)
113.070(59)	3 <sup>+</sup>	61.3(59)*	3.66(15)
115.410(63)	3 <sup>+</sup>	61.3(59)*	47.2(34)
118.900(63)	3 <sup>+</sup>	61.3(59)*	15.9(10)
119.660(64)	4 <sup>+</sup>	61.3(59)*	2.59(15)
127.640(69)	3 <sup>+</sup>	61.3(59)*	57.1(31)
129.830(70)	3 <sup>+</sup>	61.3(59)*	70.5(40)
138.170(76)	3 <sup>+</sup>	61.3(59)*	40.6(27)
143.220(72)	3 <sup>+</sup>	61.3(59)*	4.39(21)
146.550(76)	3 <sup>+</sup>	61.3(59)*	7.17(35)
148.960(77)	4 <sup>+</sup>	61.3(59)*	2.18(12)
151.280(79)	4 <sup>+</sup>	61.3(59)*	4.13(21)
155.830(81)	4 <sup>+</sup>	61.3(59)*	6.98(34)
158.780(84)	3 <sup>+</sup>	61.3(59)*	18.6(11)
164.080(85)	3 <sup>+</sup>	61.3(59)*	18.1(11)
169.530(89)	4 <sup>+</sup>	61.3(59)*	10.45(45)

TABLE V. (Continued.)

$E_\lambda$ (eV)	$J^\pi$ ( $h^-$ )	$\Gamma_{\lambda\gamma}$ (meV)	$\Gamma_{\lambda n}$ (meV)
171.430(89)	3 <sup>+</sup>	61.3(59)*	8.18(37)
175.140(100)	4 <sup>+</sup>	61.3(59)*	3.79(26)
175.980(95)	3 <sup>+</sup>	61.3(59)*	25.6(21)
181.090(97)	4 <sup>+</sup>	61.3(59)*	23.2(15)
185.580(97)	3 <sup>+</sup>	61.3(59)*	86.5(58)
193.220(102)	3 <sup>+</sup>	61.3(59)*	112.0(65)
196.770(102)	4 <sup>+</sup>	61.3(59)*	3.75(16)
203.190(112)	3 <sup>+</sup>	61.3(59)*	1.78(16)
204.730(106)	4 <sup>+</sup>	61.3(59)*	4.53(25)
217.550(115)	4 <sup>+</sup>	61.3(59)*	28.3(19)
223.530(118)	3 <sup>+</sup>	61.3(59)*	63.5(41)
228.290(123)	4 <sup>+</sup>	61.3(59)*	33.1(10)
229.800(124)	4 <sup>+</sup>	61.3(59)*	50.1(33)
236.580(129)	4 <sup>+</sup>	61.3(59)*	1.08(16)
243.370(134)	3 <sup>+</sup>	61.3(59)*	41.6(25)
244.560(134)	4 <sup>+</sup>	61.3(59)*	15.32(44)
251.570(138)	4 <sup>+</sup>	61.3(59)*	4.02(37)
256.080(137)	3 <sup>+</sup>	61.3(59)*	80.5(57)
261.750(128)	3 <sup>+</sup>	61.3(59)*	3.00(38)
265.340(95)	3 <sup>+</sup>	61.3(59)*	1.18(17)
267.250(234)	4 <sup>+</sup>	61.3(59)*	0.32(13)
274.220(149)	4 <sup>+</sup>	61.3(59)*	92.5(66)
278.160(150)	3 <sup>+</sup>	61.3(59)*	14.02(74)
282.740(154)	4 <sup>+</sup>	61.3(59)*	8.29(54)
289.240(161)	3 <sup>+</sup>	61.3(59)*	126.6(42)
292.060(161)	4 <sup>+</sup>	61.3(59)*	86.0(45)
295.430(161)	3 <sup>+</sup>	61.3(59)*	45.4(24)
305.360(160)	4 <sup>+</sup>	61.3(59)*	18.8(12)
308.240(164)	4 <sup>+</sup>	61.3(59)*	5.91(51)
314.620(169)	3 <sup>+</sup>	61.3(59)*	73.7(38)
317.710(167)	4 <sup>+</sup>	61.3(59)*	24.01(62)
319.020(172)	3 <sup>+</sup>	61.3(59)*	62.3(45)
323.340(173)	4 <sup>+</sup>	61.3(59)*	7.03(42)
325.010(180)	3 <sup>+</sup>	61.3(59)*	6.05(51)
330.920(178)	4 <sup>+</sup>	61.3(59)*	217(12)
338.940(186)	3 <sup>+</sup>	61.3(59)*	19.13(97)
341.330(202)	3 <sup>+</sup>	61.3(59)*	8.70(98)
344.190(191)	4 <sup>+</sup>	61.3(59)*	52.2(30)
348.360(191)	3 <sup>+</sup>	61.3(59)*	43.9(27)
356.540(188)	4 <sup>+</sup>	61.3(59)*	8.94(66)
359.300(184)	4 <sup>+</sup>	61.3(59)*	13.09(85)
364.840(183)	3 <sup>+</sup>	61.3(59)*	5.82(66)
367.770(191)	4 <sup>+</sup>	61.3(59)*	4.30(53)
380.200(200)	4 <sup>+</sup>	61.3(59)*	31.1(16)
383.750(203)	4 <sup>+</sup>	61.3(59)*	19.9(10)
385.900(201)	3 <sup>+</sup>	61.3(59)*	6.16(58)
392.710(209)	3 <sup>+</sup>	61.3(59)*	25.1(17)
394.080(210)	4 <sup>+</sup>	61.3(59)*	76.3(40)
399.070(218)	3 <sup>+</sup>	61.3(59)*	12.34(93)
405.800(208)	4 <sup>+</sup>	61.3(59)*	24.0(14)
407.120(217)	3 <sup>+</sup>	61.3(59)*	15.07(62)
413.640(211)	4 <sup>+</sup>	61.3(59)*	7.54(47)
419.610(218)	3 <sup>+</sup>	61.3(59)*	32.8(13)
422.940(220)	4 <sup>+</sup>	61.3(59)*	5.60(30)
428.750(226)	4 <sup>+</sup>	61.3(59)*	9.13(43)
434.900(230)	3 <sup>+</sup>	61.3(59)*	80.7(32)

TABLE V. (*Continued.*)

$E_\lambda$ (eV)	$J^\pi$ ( $h^-$ )	$\Gamma_{\lambda\gamma}$ (meV)	$\Gamma_{\lambda n}$ (meV)
439.420(234)	3 <sup>+</sup>	61.3(59)*	32.0(13)
440.820(235)	3 <sup>+</sup>	61.3(59)*	47.5(12)
444.830(238)	4 <sup>+</sup>	61.3(59)*	46.5(19)
451.700(205)	3 <sup>+</sup>	61.3(59)*	2.89(38)
455.170(230)	4 <sup>+</sup>	61.3(59)*	15.86(74)
457.760(209)	3 <sup>+</sup>	61.3(59)*	2.14(42)
467.900(243)	4 <sup>+</sup>	61.3(59)*	14.27(53)
469.630(246)	4 <sup>+</sup>	61.3(59)*	12.02(45)
474.460(247)	3 <sup>+</sup>	61.3(59)*	71.0(27)
478.430(250)	4 <sup>+</sup>	61.3(59)*	22.37(82)
485.230(256)	4 <sup>+</sup>	61.3(59)*	58.4(16)
488.650(258)	3 <sup>+</sup>	61.3(59)*	129(6)
495.300(264)	3 <sup>+</sup>	61.3(59)*	8.44(61)
500.790(262)	4 <sup>+</sup>	61.3(59)*	17.39(76)
505.380(265)	3 <sup>+</sup>	61.3(59)*	30.7(13)
512.630(270)	3 <sup>+</sup>	61.3(59)*	54.4(19)
515.850(274)	4 <sup>+</sup>	61.3(59)*	34.5(12)
520.710(276)	3 <sup>+</sup>	61.3(59)*	138.8(78)
522.730(278)	3 <sup>+</sup>	61.3(59)*	10.85(88)
528.810(284)	4 <sup>+</sup>	61.3(59)*	15.09(68)
537.360(286)	3 <sup>+</sup>	61.3(59)*	5.59(57)
540.760(292)	3 <sup>+</sup>	61.3(59)*	56.4(23)
545.910(291)	4 <sup>+</sup>	61.3(59)*	5.12(49)
550.060(268)	3 <sup>+</sup>	61.3(59)*	34.5(15)
552.260(274)	4 <sup>+</sup>	61.3(59)*	10.14(53)
564.460(280)	3 <sup>+</sup>	61.3(59)*	23.43(90)
567.400(283)	4 <sup>+</sup>	61.3(59)*	67.5(25)
571.890(286)	4 <sup>+</sup>	61.3(59)*	40.0(15)
579.300(292)	3 <sup>+</sup>	61.3(59)*	113.1(82)
581.130(309)	4 <sup>+</sup>	61.3(59)*	19.2(20)
588.990(299)	3 <sup>+</sup>	61.3(59)*	34.4(14)
593.870(299)	4 <sup>+</sup>	61.3(59)*	14.93(75)
598.180(308)	3 <sup>+</sup>	61.3(59)*	92.7(34)
602.750(307)	3 <sup>+</sup>	61.3(59)*	35.9(16)
606.410(312)	3 <sup>+</sup>	61.3(59)*	212.2(90)
616.060(322)	4 <sup>+</sup>	61.3(59)*	77.6(33)
622.460(327)	3 <sup>+</sup>	61.3(59)*	94.0(34)
626.500(333)	3 <sup>+</sup>	61.3(59)*	18.6(15)
628.680(332)	3 <sup>+</sup>	61.3(59)*	241(11)
631.490(336)	3 <sup>+</sup>	61.3(59)*	10.3(11)
634.410(336)	3 <sup>+</sup>	61.3(59)*	22.7(11)
639.990(340)	3 <sup>+</sup>	61.3(59)*	14.60(81)
650.150(350)	4 <sup>+</sup>	61.3(59)*	90.8(31)
655.460(353)	3 <sup>+</sup>	61.3(59)*	98.7(31)
658.620(355)	4 <sup>+</sup>	61.3(59)*	32.9(19)
660.150(351)	3 <sup>+</sup>	61.3(59)*	23.8(21)
668.160(356)	4 <sup>+</sup>	61.3(59)*	7.17(72)
672.600(361)	3 <sup>+</sup>	61.3(59)*	60.5(22)
678.320(358)	4 <sup>+</sup>	61.3(59)*	20.8(11)
683.050(364)	3 <sup>+</sup>	61.3(59)*	46.0(18)
687.300(366)	4 <sup>+</sup>	61.3(59)*	48.6(19)
693.830(370)	3 <sup>+</sup>	61.3(59)*	107.3(49)
698.000(371)	4 <sup>+</sup>	61.3(59)*	6.97(85)
700.260(376)	3 <sup>+</sup>	61.3(59)*	18.7(12)
706.340(381)	3 <sup>+</sup>	61.3(59)*	43.3(21)

TABLE V. (*Continued.*)

$E_\lambda$ (eV)	$J^\pi$ ( $h^-$ )	$\Gamma_{\lambda\gamma}$ (meV)	$\Gamma_{\lambda n}$ (meV)
719.180(392)	3 <sup>+</sup>	61.3(59)*	73.7(28)
725.060(395)	4 <sup>+</sup>	61.3(59)*	42.3(14)
727.300(396)	4 <sup>+</sup>	61.3(59)*	61.0(26)
737.670(393)	3 <sup>+</sup>	61.3(59)*	8.5(11)
741.080(408)	4 <sup>+</sup>	61.3(59)*	29.6(14)
751.920(379)	3 <sup>+</sup>	61.3(59)*	75.8(34)
755.170(379)	3 <sup>+</sup>	61.3(59)*	38.1(17)
760.500(200)	4 <sup>+</sup>	61.3(59)*	6.43(95)
762.730(347)	4 <sup>+</sup>	61.3(59)*	20.4(15)
767.100(198)	4 <sup>+</sup>	61.3(59)*	7.67(98)
769.550(377)	3 <sup>+</sup>	61.3(59)*	118.1(58)
775.940(397)	4 <sup>+</sup>	61.3(59)*	10.70(64)
779.060(401)	4 <sup>+</sup>	61.3(59)*	43.7(18)
784.910(405)	3 <sup>+</sup>	61.3(59)*	25.8(14)
793.220(413)	3 <sup>+</sup>	61.3(59)*	24.0(14)
796.280(424)	4 <sup>+</sup>	61.3(59)*	28.0(16)
798.400(419)	3 <sup>+</sup>	61.3(59)*	63.3(32)
802.780(427)	3 <sup>+</sup>	61.3(59)*	70.8(28)
805.070(423)	3 <sup>+</sup>	61.3(59)*	202(11)
819.850(436)	4 <sup>+</sup>	61.3(59)*	9.07(83)
822.710(435)	4 <sup>+</sup>	61.3(59)*	40.1(14)
826.910(438)	4 <sup>+</sup>	61.3(59)*	15.80(76)
831.480(442)	3 <sup>+</sup>	61.3(59)*	58.6(21)
834.150(444)	3 <sup>+</sup>	61.3(59)*	77.7(26)
838.390(450)	3 <sup>+</sup>	61.3(59)*	24.60(86)
841.650(450)	4 <sup>+</sup>	61.3(59)*	113.5(40)
845.560(455)	4 <sup>+</sup>	61.3(59)*	37.4(13)
857.970(42)	3 <sup>+</sup>	61.3(59)*	181.8(93)
863.380(43)	3 <sup>+</sup>	61.3(59)*	95.4(68)
864.830(43)	4 <sup>+</sup>	61.3(59)*	106.4(83)
868.170(44)	3 <sup>+</sup>	61.3(59)*	32.6(19)
876.690(45)	3 <sup>+</sup>	61.3(59)*	16.7(12)
880.060(44)	4 <sup>+</sup>	61.3(59)*	58.3(29)
886.130(44)	4 <sup>+</sup>	61.3(59)*	15.5(10)
890.750(44)	3 <sup>+</sup>	61.3(59)*	60.0(31)
895.760(44)	3 <sup>+</sup>	61.3(59)*	38.2(20)
900.040(45)	3 <sup>+</sup>	61.3(59)*	39.1(27)
905.280(20)	4 <sup>+</sup>	61.3(59)*	20.7(20)
907.330(40)	4 <sup>+</sup>	61.3(59)*	63.3(38)
911.780(46)	3 <sup>+</sup>	61.3(59)*	98.1(49)
915.540(46)	3 <sup>+</sup>	61.3(59)*	36.4(23)
924.290(47)	4 <sup>+</sup>	61.3(59)*	110.3(57)
931.110(47)	3 <sup>+</sup>	61.3(59)*	83.9(51)
933.390(204)	3 <sup>+</sup>	61.3(59)*	16.5(18)
942.250(48)	4 <sup>+</sup>	61.3(59)*	163.2(74)
946.360(47)	4 <sup>+</sup>	61.3(59)*	64.8(29)
956.750(47)	3 <sup>+</sup>	61.3(59)*	17.8(17)
962.390(47)	3 <sup>+</sup>	61.3(59)*	130.8(72)
967.110(47)	3 <sup>+</sup>	61.3(59)*	138.3(72)
970.380(47)	3 <sup>+</sup>	61.3(59)*	58.5(33)
976.470(48)	4 <sup>+</sup>	61.3(59)*	28.7(18)
986.150(48)	3 <sup>+</sup>	61.3(59)*	23.5(19)
989.000(48)	4 <sup>+</sup>	61.3(59)*	17.2(17)
991.620(48)	4 <sup>+</sup>	61.3(59)*	55.7(32)

TABLE VI. Capture ( $\sigma_Y^{th}$ ), elastic ( $\sigma_n^{th}$ ), and total ( $\sigma_{tot}^{th}$ ) cross sections recommended by Mughabghab [5] at the thermal neutron energy ( $E_{th} = 25.3$  meV).

	$^{175}\text{Lu}$	$^{176}\text{Lu}$	$^{nat}\text{Lu}$
$\sigma_Y^{th}$	23.3(11) b	2020(70) b	74.9(20) b
$\sigma_n^{th}$	6.7(4) b	5.6(3) b	6.79(8) b
$\sigma_{tot}^{th}$	30(1) b		

on the choice of the cutoff energy  $E_{cut} = 50$  eV are given in Sec. IV B.

### C. Results and discussions

The parameters of the bound (negative) resonance reported on top of Table V have been fine tuned to reproduce the thermal neutron cross sections as listed in Table VI. They strongly depend on the shape of the first  $^{176}\text{Lu}$  resonance, located close to the thermal energy at 0.143 eV. The energy, neutron width, and radiation width of this resonance have been derived from the data of Table II, measured with natural and enriched samples. Figure 2 compares the experimental cross sections with theoretical curves provided by the REFIT code below 1 eV. These results were obtained with an effective scattering radius  $R' = 7.9(2)$  fm. The latter parameter defines the shape-elastic cross section, that becomes the potential scattering cross section at low incident neutron energy. In the present work, it was provided by optical model calculations. Origins of this value are explained in Sec. V A.

Transmission data listed in Table IV have been included in the resonance analysis for determining parameters of the unbound states above 1 eV. Theoretical curves and experimental values measured at the GELINA and DANCE facilities are compared in Fig. 3. The green solid curve represents the contribution of the  $^{181}\text{Ta}$  resonances. Their impacts on the  $^{175}\text{Lu}$  resonance parameters have been studied by decreasing by 10% the areal density of tantalum. Figure 4 shows that the ratios of the  $^{175}\text{Lu}$  neutron and radiation widths obtained with and without the perturbation of the  $^{181}\text{Ta}$  areal density remain close to unity, indicating the low impact of  $^{181}\text{Ta}$  on the final results.

Including in the analysis the transmission data (thin sample) of Liou *et al.* was not straightforward. As shown in Fig. 5, experimental biases are highlighted by the energy-dependent residuals  $r$  between the theoretical  $\mathcal{T}_{th}$  and experimental  $\mathcal{T}_{exp}$  transmissions, weighted by the experimental uncertainties  $u_{\mathcal{T}_{exp}}$ :

$$r(t) = \left( \frac{\mathcal{T}_{th}(t) - \mathcal{T}_{exp}(t)}{u_{\mathcal{T}_{exp}}(t)} \right)^2. \quad (4)$$

Few structures located at the resonance energies can be observed below 20 eV in the residuals shown in the middle plot of Fig. 5. Such structures cannot be explained by missing small resonances because the prior  $^{175}\text{Lu}$  resonances introduced in the calculations come from the work of Liou *et al.* Sample inhomogeneities could better explain them. The bottom plot in Fig. 5 shows that the use of a log-normal

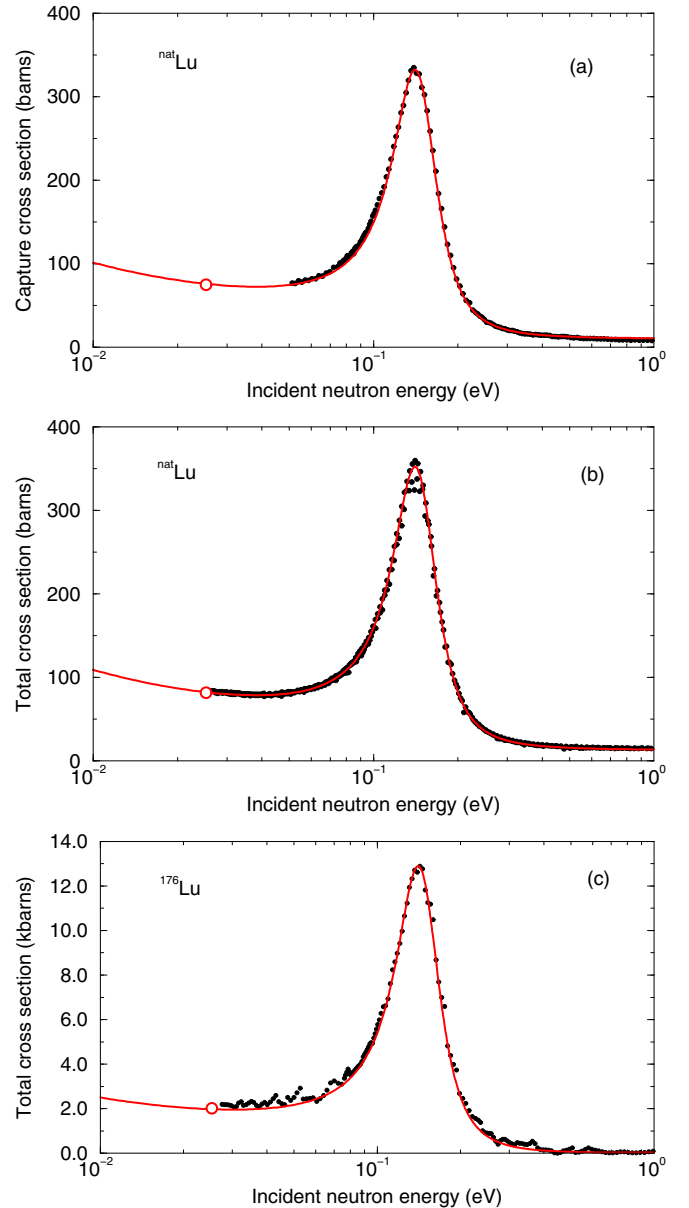


FIG. 2. First  $^{176}\text{Lu}$  resonance at 0.143 eV observed from the data sets listed in Table II. The top and middle plots (a),(b) represent the natural Lu capture and total cross sections, respectively. The bottom plot (c) shows the  $^{176}\text{Lu}$  total cross section. The open circles indicate the thermal cross sections at 25.3 meV recommended by Mughabghab [5]. The red solid lines were obtained with the resonance parameters provided by the REFIT code.

distribution in the REFIT code, to account for grain size effects in the sample, smoothens the observed structures. Such experimental issues and their consequences on the determination of the radiation widths are discussed in Refs. [29,30]. As no trustable corrections can be applied, data from Liou *et al.* measured with the thin sample were only used in a narrow energy interval, ranging from 18 to 44 eV.

Figure 6 shows that many structures can still be distinguished above 700 eV in the transmission data measured at the GELINA facility with the 2-mm-thick natural lutetium

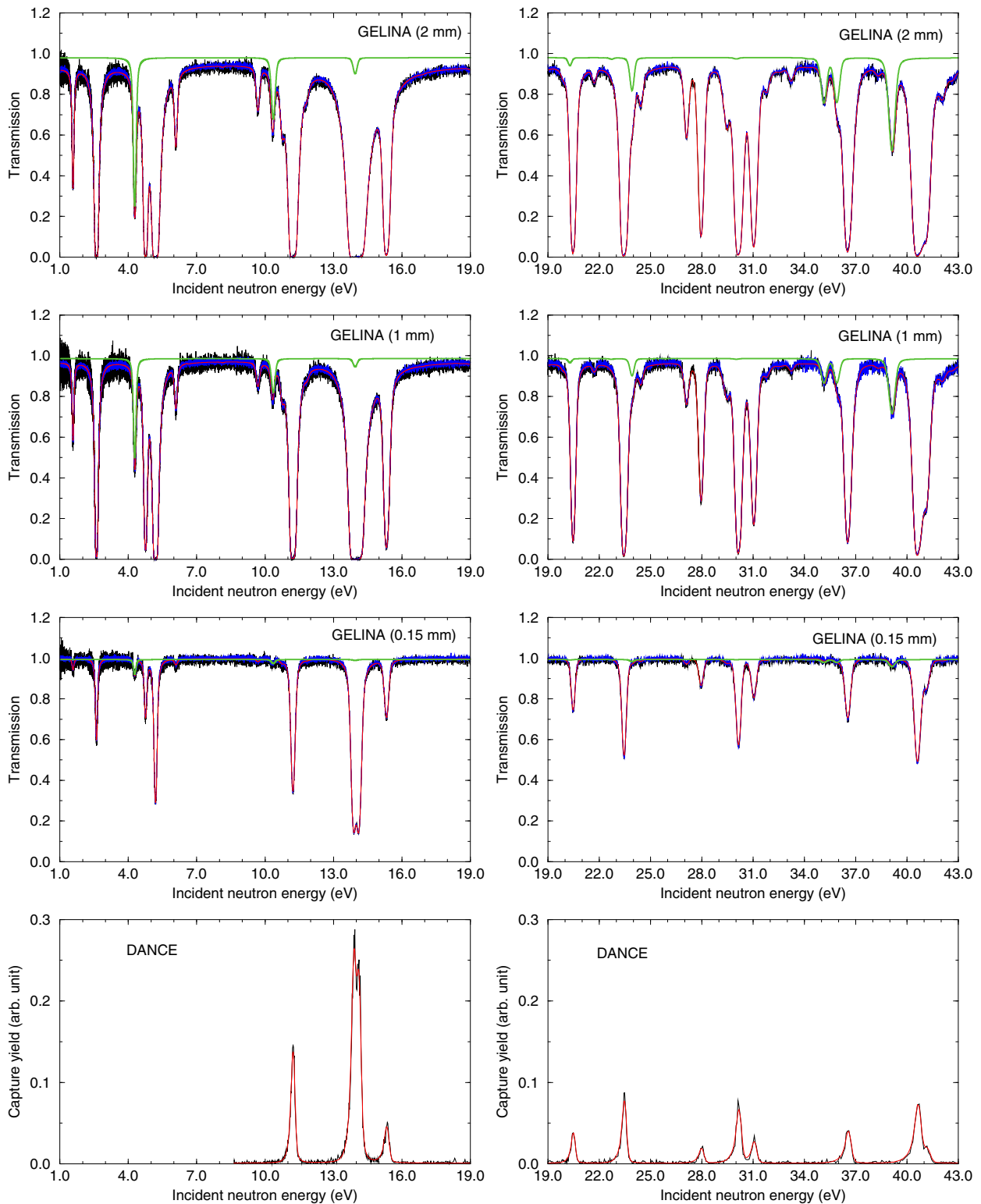


FIG. 3. Transmission measured at the GELINA facility with natural Lu samples and capture data measured at the DANCE facility with an enriched  $^{175}\text{Lu}$  sample. For the transmission experiments, the black (blue) solid lines represent the data obtained with a boron (cadmium) antioverlap filter. The red solid line represents the final results provided by the REFIT code below 43 eV. The green solid line shows the  $^{181}\text{Ta}$  contribution in the transmission data.



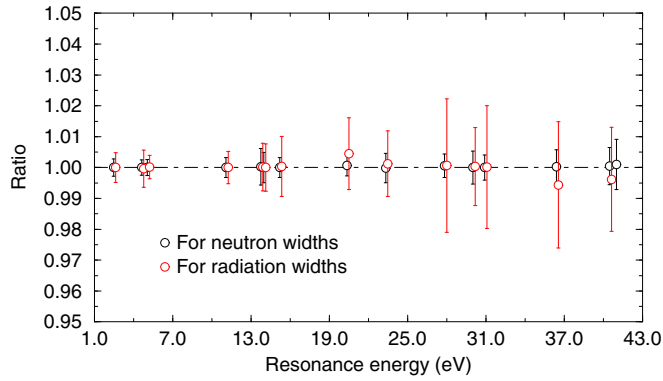


FIG. 4. Ratios of the  $^{175}\text{Lu}$  neutron and radiation widths obtained with and without a 10% perturbation of the  $^{181}\text{Ta}$  areal density below 43 eV.

sample. However, the short flight path length ( $L = 10.861$  m) provides low-resolution data. In that case, data from Liou *et al.* measured with a thick  $^{175}\text{Lu}$  sample at  $L = 202.05$  m provide a unique high-resolution transmission data set that allows one to separate  $s$ -wave resonances beyond 1 keV. Many structures can be observed even between the resonances; they can be attributed either to small  $p$ -wave resonances or statistical fluctuations. As the present work focuses on the  $s$ -wave properties of the  $^{175}\text{Lu} + n$  compound system, we did not attempt to refine the description of these small structures.

In Table V, quoted uncertainties were calculated with a Monte Carlo technique [31] by randomly varying experimental parameters, assuming they are normally distributed. Thousand REFIT calculations were repeated and uncertainties of about seventy experimental parameters have been propagated to resonance parameter uncertainties. We used uncer-

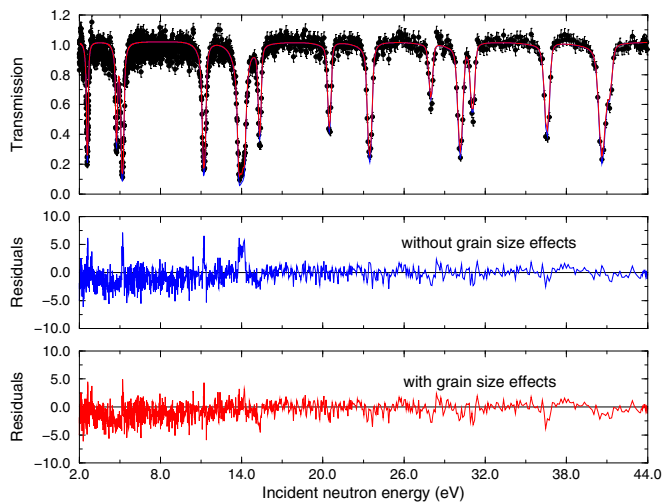


FIG. 5. Transmission measured by Liou *et al.* [7] at the 39.57 m flight path of the Columbia University Nevis synchrocyclotron with a thin sample of  $\text{Lu}_2\text{O}_3$  enriched to 99.926% in  $^{175}\text{Lu}$  ( $1.425 \times 10^{-3}$  atom/barn). The blue and red lines represent the REFIT results calculated without and with inhomogeneities due to grain size effects in the sample. Residuals are calculated with Eq. (4).

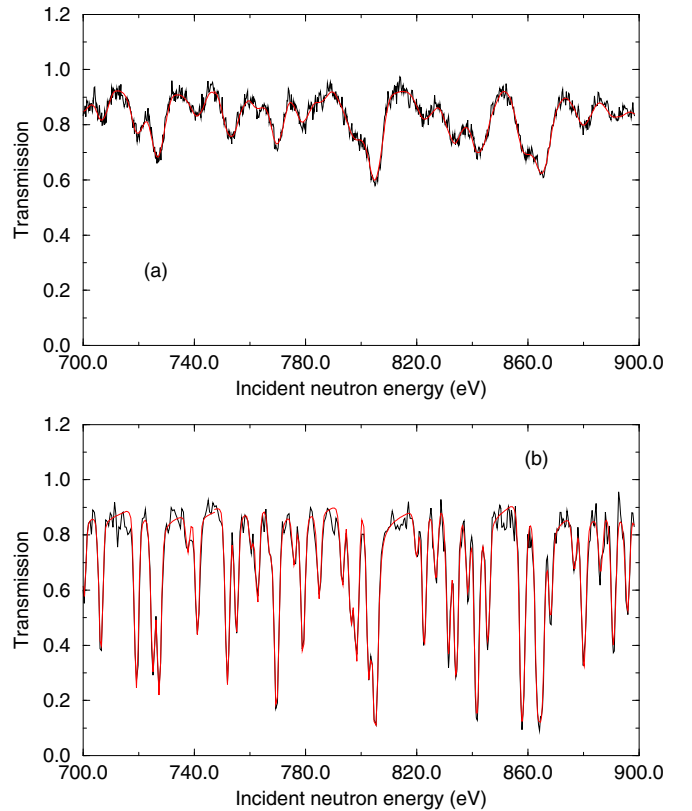


FIG. 6. The top plot (a) shows the transmission measured at the GELINA facility with the thick natural Lu samples (2 mm) at  $L = 10.861$  m. The bottom plot (b) shows the transmission measured by Liou *et al.* with an enriched  $^{175}\text{Lu}$  thick sample at  $L = 202.05$  m. The red line represents the final results provided by the REFIT code between 700 and 900 eV.

tainties close to  $\pm 3.5\%$  on the normalization factor of the capture yields, temperature uncertainties ranging from 1 to 5 K, and areal density uncertainties of 2–3%. Uncertainties on the parameters of the analytic response function are not well known. In the present work, they were optimized to set up a conservative uncertainty of  $\simeq 10\%$  on the full width at half maximum (FWHM) of the time-dependent distributions. Figure 7 indicates that increasing the FWHM uncertainty above 10% creates structures in the residuals which are no longer compatible with the transmission data measured at the GELINA facility with the thick lutetium sample (2 mm). In practice, the final resonance parameter uncertainties are dominated by the normalization and areal density uncertainties.

#### IV. AVERAGE s-WAVE RESONANCE PARAMETERS

Average  $s$ -wave resonance parameters were established from the statistical analysis of the resonance parameters established in this work. Several statistical approaches are available and well documented in the literature. In the present work, we have used the ESTIMA method [32] to determine simultaneously the  $s$ -wave mean level spacing  $D_0$  and neutron strength function  $S_0$ . The average radiation width  $\langle \Gamma_{\gamma_0} \rangle$  results

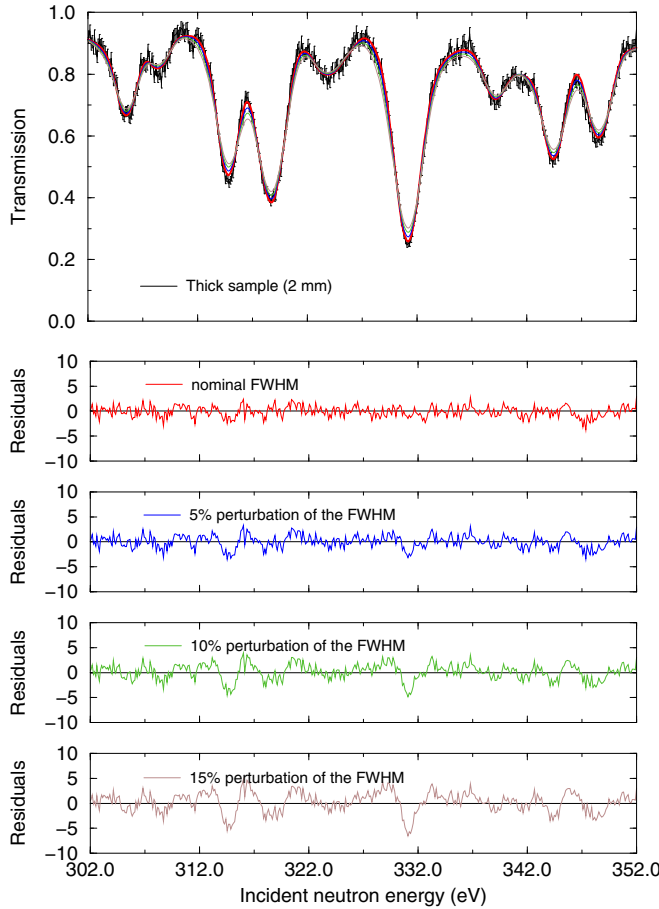


FIG. 7. Impact of the response function on the theoretical transmission calculated between 302 and 352 eV for the thick sample measured at the GELINA facility. Results obtained for the nominal value of the full width at half maximum (FWHM) of the response function are compared with those obtained from perturbations of 5%, 10%, and 15% of the FWHM. Residuals are calculated with Eq. (4).

from the average of the individual radiation widths reported in Table V.

### A. Mean level spacing and neutron strength function

The statistical method implemented in the ESTIMA code was designed to determine  $D_0$  and  $S_0$  by taking into account contributions of missing levels. The method relies on the probability density function of the reduced neutron widths hypothesized by Porter and Thomas [18], which is a chi-squared function with one degree of freedom:

$$P(x) = \frac{e^{-x/2}}{\sqrt{2\pi x}}. \quad (5)$$

The dimensionless variable  $x$  is the ratio of the reduced neutron widths  $\Gamma_{\lambda,n}^l$  weighted by the statistical spin factor  $g_J$  to its average value:

$$x = \frac{g_J \Gamma_{\lambda,n}^l}{\langle g_J \Gamma_{\lambda,n}^l \rangle}. \quad (6)$$

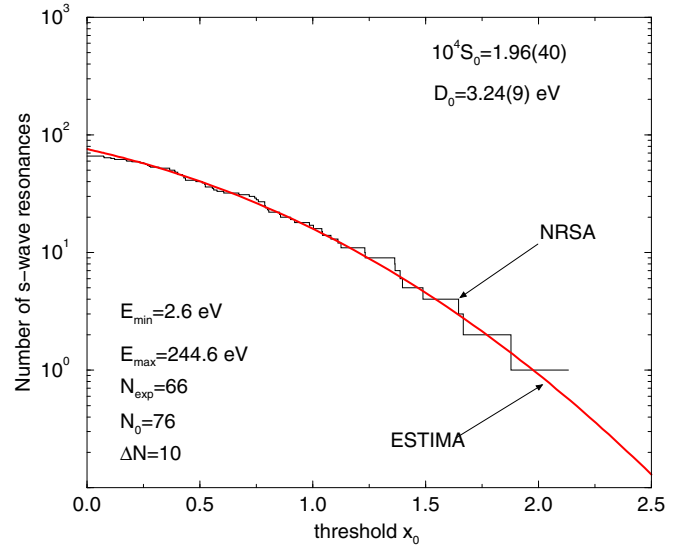


FIG. 8. ESTIMA results obtained for the compound system  $^{175}\text{Lu} + n$  compared to the cumulative distribution function of the Porter-Thomas law.  $E_{\min}$  and  $E_{\max}$  stand for the lower and upper limit of the energy range in which the average resonance parameters have been obtained [see Eq. (10)].

For the  $s$  wave ( $l = 0$ ), the definition of the reduced neutron width is

$$\Gamma_{\lambda,n}^0 = \Gamma_{\lambda,n} \sqrt{\frac{1 \text{ eV}}{E_{\lambda}}}, \quad (7)$$

and its average value is related to the mean level spacing and neutron strength function as follows:

$$\langle g_J \Gamma_{\lambda,n}^0 \rangle = S_0 D_0. \quad (8)$$

A common method which accounts for missing levels in the statistical treatment of the resonance parameters consists of computing the cumulative distribution function of the Porter-Thomas law:

$$N(x_0) = N_0 \int_{x_0}^{\infty} P(x) dx = N_0 \operatorname{erfc} \left( \sqrt{\frac{x_0}{2}} \right), \quad (9)$$

in which  $N(0) = N_0$  represents the number of estimated levels at  $x_0 = 0$ . The  $s$ -wave mean level spacing  $D_0$  is then calculated as follows:

$$D_0 = \frac{E_{\max} - E_{\min}}{N_0 - 1}. \quad (10)$$

Energies  $E_{\min}$  and  $E_{\max}$  represent the lower and upper energy limits of the resolved resonance range under investigation. In ESTIMA,  $N_0$  and  $\langle g_J \Gamma_{\lambda,n}^0 \rangle$  are free parameters. The neutron strength function and mean level spacing are calculated with Eqs. (8) and (10).

ESTIMA results are shown in Fig. 8. For the compound system  $^{175}\text{Lu} + n$ , a good agreement between the theoretical and experimental distributions  $N(x_0)$  is obtained with

$$\begin{aligned} 10^4 S_0 &= 1.96(40), \\ D_0 &= 3.24(9) \text{ eV}. \end{aligned}$$

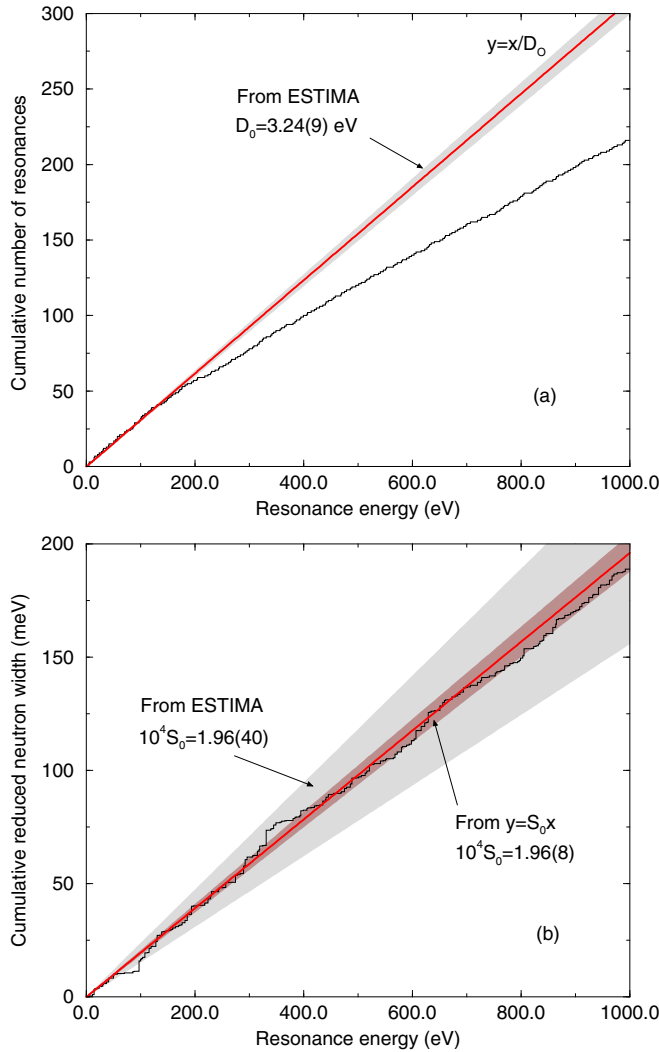


FIG. 9. Staircase plots of the cumulative number of  $s$ -wave resonances (a) and  $s$ -wave reduced neutron widths (b) compared to the ESTIMA results. For (b), a lower uncertainty is achieved from the least-squares fit of the slope of the cumulative  $s$ -wave reduced neutron widths.

The ESTIMA results are compared with those of the resonance analysis in Figs. 9(a) and 9(b). The staircase plot of the cumulated number of resonances indicates that experimentally observed resonances deviate from theory above 200 eV and reveal an increasing number of missing resonances. The staircase plot of the reduced neutron widths indicates that most of the missing levels are small resonances whose contributions to the neutron strength function are rather negligible, at least up to 800 eV. Figure 9(b) also shows that ESTIMA provides a neutron strength function with a too high uncertainty. By imposing the same lower and upper energy limits ( $E_{\min} = 2.6$  eV and  $E_{\max} = 244.6$  eV) as used in the ESTIMA analysis, a similar  $S_0$  value with a lower uncertainty close to 5% can be obtained from the least-squares fit of the slope of the cumulative reduced neutron widths as a function of the resonance energies:

$$10^4 S_0 = 1.96(8).$$

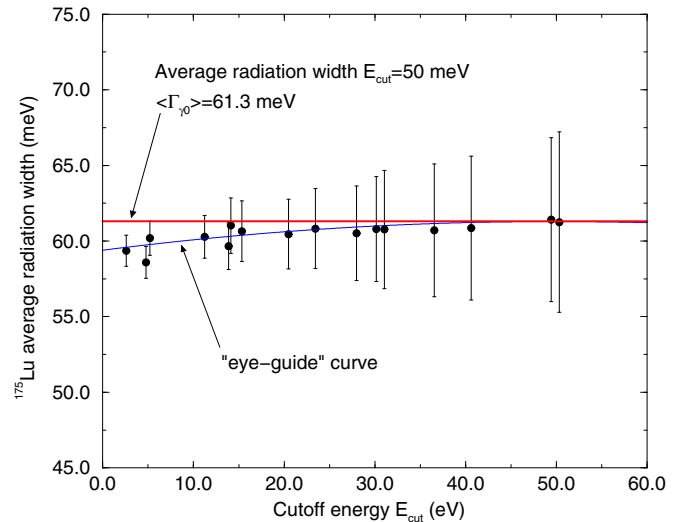


FIG. 10. Behavior of the  $^{175}\text{Lu}$  average radiation width as a function of the cutoff energy  $E_{\text{cut}}$  compared to the value obtained at  $E_{\text{cut}} = 50$  eV. The blue line is an “eye-guide” curve that follow the trends of the average values.

The above quoted uncertainty was obtained from the Monte Carlo propagation of the resonance parameters uncertainties, taking into account correlations.

As shown in Table I, the  $^{175}\text{Lu}$  average resonance parameters recommended in the literature are quite different from those found in this work. The mean level spacing  $D_0$  is between the RIPL-2 (3.0 eV) and RIPL-3 (3.45 eV) recommended values, confirming that the value of RIPL-1 was erroneous. Our statistical analysis provides an uncertainty which is slightly lower than  $\pm 3\%$ . For the  $s$ -wave neutron strength function, agreement with the value of RIPL-3 ( $1.82 \times 10^{-4}$ ) is within the limit of the quoted uncertainty. Our result mainly confirms the successive increase of  $S_0$  since the first release of the Reference Input Parameter Library RIPL-1 in 1998.

### B. Average radiation width

Assessment of reliable estimations of average radiation widths from time-of-flight data is subject to debate. Their values are usually deduced from individual radiation widths  $\Gamma_{\lambda,\gamma}$  that can be characterized by a large spread. Liou *et al.* pointed out this issue. For  $^{175}\text{Lu}$ , values of  $\Gamma_{\lambda,\gamma}$  from 59(20) to 100(20) meV were obtained for 40 levels. The average value of  $\langle \Gamma_{\gamma_0} \rangle = 77$  meV was reported without uncertainty.

In the present work, values of  $\Gamma_{\lambda,\gamma}$  from 57.2 to 69.4 meV have been deduced from 16 resonances below 50 eV. This cutoff energy limit  $E_{\text{cut}}$  is somewhat arbitrary. Figure 10 shows the behavior of the  $^{175}\text{Lu}$  average radiation width as a function of  $E_{\text{cut}}$ . A reasonable average value seems to be reached between 30 and 50 meV. Moreover, in our least-squares fit, sensitivities to  $\Gamma_{\lambda,\gamma}$  decrease as neutron energy increases, so that, above  $E_{\text{cut}} = 50$  eV, their uncertainties increase significantly and values provided by REFIT are less trustable.

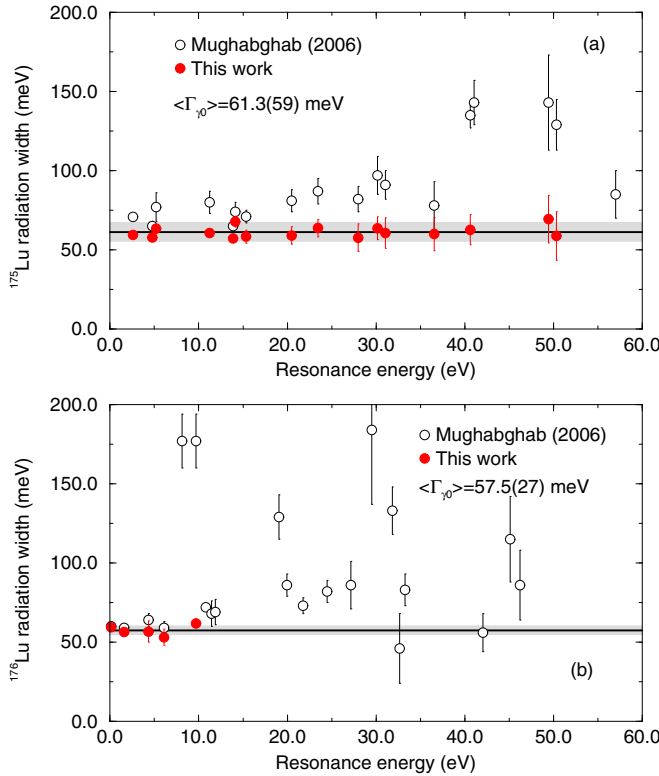


FIG. 11. Individual  $^{175}\text{Lu}$  and  $^{176}\text{Lu}$  radiation widths obtained in this work and compared with those reported in Ref. [5].

The individual  $^{175}\text{Lu}$  radiation widths are reported in Fig. 11(a). For comparison, those obtained for only five  $^{176}\text{Lu}$  resonances below 10 eV are given in Fig. 11(b). The large spread of the radiation widths compiled by Mughabghab in Ref. [5] is not confirmed by the present results. The average values

$$\langle \Gamma_{\gamma_0} \rangle (A = 175) = 61.3(59) \text{ meV}$$

and

$$\langle \Gamma_{\gamma_0} \rangle (A = 176) = 57.7(27) \text{ meV}$$

are the two first moments of the distributions obtained from the Monte Carlo propagation of the resonance parameter uncertainties, taking into account correlations. An example of distribution obtained for  $^{175}\text{Lu}$  is shown in Fig. 12. The value of 61.3 meV is substantially lower than the mean value of 77 meV reported by Liou *et al.* The quoted relative uncertainty of 9.6% cannot confirm such a high value. As for  $^{175}\text{Lu}$ , a lower  $^{176}\text{Lu}$  average radiation width of 57.7 meV is suggested in comparison to 63 and 66 meV reported by Mughabghab [5] and Roig *et al.* [12], respectively.

A method for estimating average radiation widths was proposed in Ref. [33] and applied to xenon isotopes from  $A = 124$  to  $A = 136$ . The purpose was to make predictions for a given isotope for which prior model parameters (level density parameter and average radiation width) are revised accordingly to posterior results previously established for neighboring isotopes. If we assume that the total  $\gamma$ -ray decay to low lying-states is dominated by a given  $XI$  radiation, the

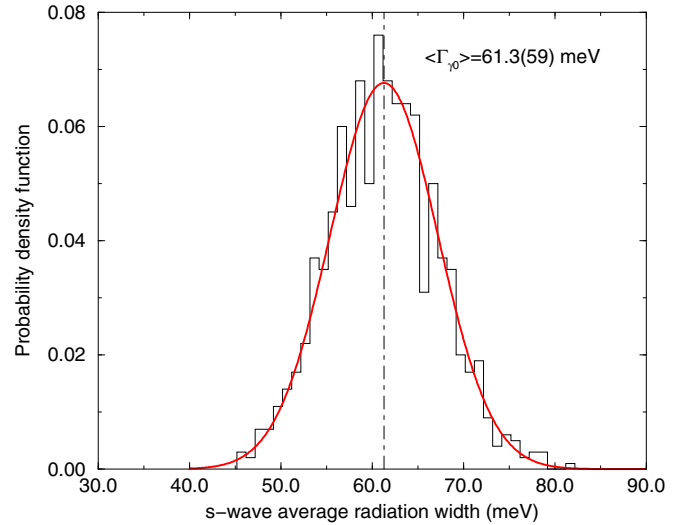


FIG. 12. Distribution of the  $^{175}\text{Lu}$  average radiation width ( $\Gamma_{\gamma_0}$ ) obtained from the Monte Carlo propagation of the resonance parameter uncertainties, taking into account correlations.

$s$ -wave average radiation width at excitation energy close to  $S_n$  is given by

$$\langle \Gamma_{\gamma_0} \rangle_{th} \simeq D_0 \int_0^{S_n} E_\gamma^3 f_{Xl}(E_\gamma) \sum_{I=J-1}^{J+1} \rho_I(S_n - E_\gamma) dE_\gamma, \quad (11)$$

in which the spectral factor  $f_{Xl}$  is related to giant dipole resonance (GDR) modes in photoabsorption cross section and  $\rho_J$  stands for the  $J$ -dependent level density. The average radiation width ( $\Gamma_{\gamma_0}$ )<sub>th</sub> was determined at  $S_n$  with experimental and theoretical constraints (level density parameter,  $\gamma$ -ray strength function, and cumulated number of low-lying nuclear levels). In this work, prior information for the level density parameters and  $\gamma$ -ray strength functions were established by using various nuclear models and parametrizations available in the TALYS code [19]. At the end of a recursive process, we have obtained a set of model-dependent parameters ( $\Gamma_{\gamma_0}$ )<sub>thi</sub>, whose mean value can provide valuable revised information for the neighboring isotopes. This approach can be only applied at low incident neutron energy, where the average properties of the neutron resonance parameters exhibit negligible neutron energy dependence.

A local systematic for lutetium was calibrated starting from the mean level spacing (3.24 eV) and average radiation width (61.3 meV) of the compound system  $^{175}\text{Lu} + n$ . For the level density, we have used the composite formula of Gilbert and Cameron [34] with a constant level density parameter  $a$ . The behavior of the level density parameter with the mass of the compound nucleus was deduced from phenomenological models (back-shifted Fermi gas model, generalized superfluid model) and microscopic level density tables. Single and generalized Lorentzian expressions were used in the GDR models [Eq. (11)]. Figure 13 shows the distribution of ( $\Gamma_{\gamma_0}$ )<sub>thi</sub> for the compound system  $^{176}\text{Lu} + n$  obtained from random combinations of different nuclear models. The two structures mainly originate from different parametrizations of the back-shifted

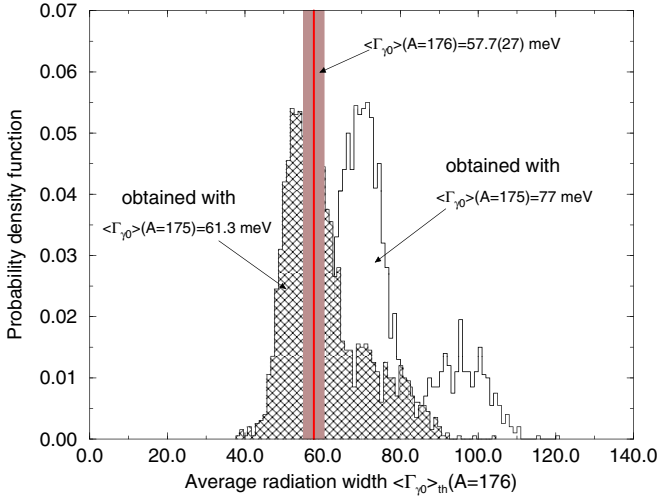


FIG. 13. Distribution of the  $^{176}\text{Lu}$  average radiation widths  $\langle \Gamma_{\gamma_0} \rangle_{th}$  predicted from the combination of different models, starting from the  $^{175}\text{Lu}$  average radiation width obtained in this work (61.3 meV) and that reported in the literature (77 meV). Results are compared to the  $^{176}\text{Lu}$  average radiation width [57.2(27) meV] obtained from the resonance analysis.

Fermi gas and generalized superfluid models. The mean value,

$$\langle \Gamma_{\gamma_0} \rangle_{th}(A = 176) = 60.2(10) \text{ meV},$$

is in good agreement with an average radiation width of 57.7 meV deduced from the resonance analysis. The same calculations were repeated by increasing the  $^{175}\text{Lu}$  average radiation width up to 77 meV. The mean value of the random results, shown in Fig. 13, is equal to

$$\langle \Gamma_{\gamma_0} \rangle_{th}(A = 176) = 76.0(12) \text{ meV}.$$

This result is not compatible either with our value of 57.7 meV or with the low energy values ( $E < 10$  eV) reported by Mughabghab [Fig. 11(b)]. A  $^{175}\text{Lu}$  average radiation width lower than 77 meV is then expected, which tends to confirm results found in this work.

The random combination of level density and GDR models carries limitations, mainly because calculations are based on a selected set of nuclear models that can only provide quantitative feedback on the expected values of the average parameters. Improved theoretical predictions of the average radiation widths for the lutetium isotopes could be achieved using an  $M1$  scissors mode in the GDR model of the  $\gamma$ -ray strength function, as was recently done by Goriely *et al.* [35] on the basis of experimental and theoretical works published in the last few years.

## V. AVERAGE NEUTRON CROSS SECTIONS

The  $^{175}\text{Lu}$  neutron induced cross sections above 1 keV were calculated with the TALYS code, by introducing in the optical and statistical model calculations the  $s$ -wave average parameters  $S_0 = 1.96 \times 10^{-4}$ ,  $D_0 = 3.24$  eV, and  $\langle \Gamma_{\gamma_0} \rangle = 61.3$  meV. The aim of this section is to discuss the agreement

between the experimental and theoretical total and capture cross sections in the neutron energy range dominated by the  $s$ -wave channel.

### A. Optical model calculations

The total cross section linearly depends on the real part of the scattering matrix  $S_{IJ}$ :

$$\sigma_{\text{tot},IJ}(E) = \frac{2\pi}{k^2} g_J \{1 - \text{Re}[S_{IJ}(E)]\}, \quad (12)$$

where  $S_{IJ}$  can be expressed for further convenience through the diagonal  $C$  matrix:

$$S_{IJ} = 1 + 2iC_{IJ}. \quad (13)$$

Elements  $C_{IJ}$  are calculated by solving the Schrodinger equation for a given complex mean-field optical model potential. The depth, radius, and diffuseness of the surface, volumic, and spin-orbit potentials are free parameters, which are adjusted on neutron cross sections. The  $s$ -wave neutron strength function can be introduced as a constraint in the minimization procedure, by using the following relationship [36]:

$$\pi S_0 \sqrt{E} = \frac{4(\beta_0 - \theta_0^2)}{1 + 2\theta_0^2 - 2\beta_0 + (1 - 2\beta_0) \cos[2\phi_0] - 2\alpha_0 \sin[2\phi_0]}. \quad (14)$$

Parameters  $\alpha_0$ ,  $\beta_0$ , and  $\theta_0$  represent the real part  $\text{Re}[C_0]$ , the imaginary part  $\text{Im}[C_0]$ , and the absolute value  $|C_0|$  of the  $C$ -matrix elements for  $l = 0$ . In the framework of the equivalent hard-sphere scattering radius approximation [37], the optical model phase shift  $\phi_0$  involved in the denominator of Eq. (14) is related to the effective scattering radius  $R'$  times the neutron wave number  $k$ :

$$\phi_0(E) = kR'. \quad (15)$$

The effective scattering radius is given by the shape-elastic cross section, that becomes the potential scattering cross section at low energy:

$$\sigma_p = 4\pi R'^2. \quad (16)$$

For modeling neutron-induced reactions on the deformed lutetium nuclei, coupled-channel calculations were performed with the ECIS module [38] of TALYS, using the rigid rotor approximation with optical model parameters established by Morillon *et al.* [39] for target mass ranging from  $A = 24$  to 209. Five ground-state rotational band states ( $7/2^+$ ,  $9/2^+$ ,  $11/2^+$ ,  $13/2^+$ ,  $15/2^+$ ) were included in the coupled-channel calculations. Prior deformation parameters  $\beta_2 = 0.287$  and  $\beta_4 = -0.069$  were retrieved from the Moller and Nix database [40]. They were slightly adjusted to 0.24 and  $-0.05$  in order to get an  $s$ -wave neutron strength function nearly equal to the value suggested by the ESTIMA analysis (Sec. IV A).

Figure 14 shows the  $^{175}\text{Lu}$  shape-elastic cross section calculated with ECIS as a function of the incident neutron energy. Its extrapolation to  $S_n$  provides  $\sigma_p$  [Eq. (16)] from which we have obtained an effective radius  $R' = 7.9(2)$  fm. This



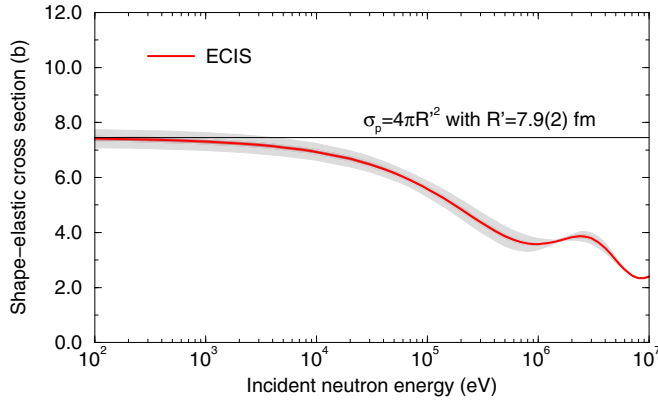


FIG. 14.  $^{175}\text{Lu}$  shape-elastic cross section calculated with the ECIS code. At low energy, the shape-elastic cross section becomes the potential scattering cross section [Eq. (16)] from which we obtain an effective radius  $R' = 7.9$  fm. The shadow area represents the uncertainty band solely due to the neutron strength function uncertainty.

value was included in the resonance analysis to determine the parameters of the bound resonance needed to reproduce the thermal cross sections (Sec. III C).

Figure 15 compares the theoretical total cross section of ECIS with data reported in the EXFOR database. Liou *et al.* did not provide to EXFOR an average total cross section corresponding to its measurement performed with the thick sample. Therefore, the transmission data (thick sample only) from Liou *et al.* were converted in total cross section, averaged over a broad energy mesh, and corrected for resonance self-shielding effect. A similar treatment was applied to the transmission measured at the GELINA facility with the thick natural Lu sample (2 mm). The reasonable agreement achieved in the keV energy range confirms the  $S_0$  value provided by the statistical analysis of the resonance parameters. Above 10 keV, performances reached by our optical model calculations are rather difficult to state since uncertainties as large as 24% are reported by Wisshak *et al.* [20].

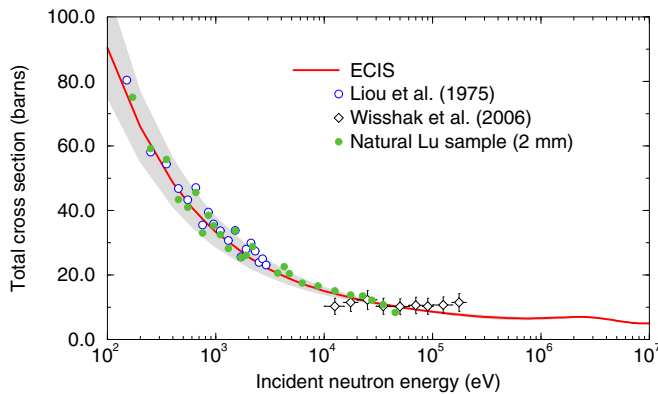


FIG. 15.  $^{175}\text{Lu}$  total cross section calculated with the ECIS code, compared with data measured by Liou *et al.* [7] and Wisshak *et al.* [20], and those deduced from the transmission measured with the thick natural Lu sample (2 mm). The shadow area represents the uncertainty band solely due to the neutron strength function uncertainty.

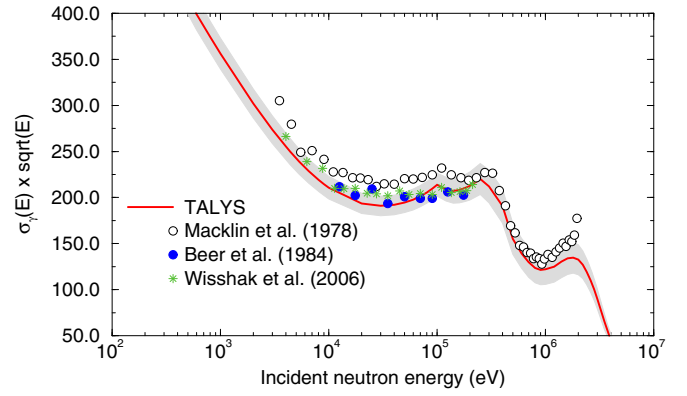


FIG. 16.  $^{175}\text{Lu}$  capture cross section times the square root of the incident neutron energy calculated with the TALYS code and compared with data measured by Wisshak *et al.* [20], Macklin *et al.* [21], and Beer *et al.* [22]. The shadow area represents the uncertainty band only due to the  $s$ -wave mean level spacing and average radiation width uncertainties.

## B. $(n, \gamma)$ reaction

The average radiative capture cross section is calculated with the TALYS code by means of the Hauser-Feshbach formula with width fluctuation corrections [41,42]:

$$\sigma_{\gamma_{IJ}} = \frac{\pi}{k^2} g_J \frac{T_{n_{IJ}} T_{\gamma_{IJ}}}{\sum_{\beta} T_{\beta_{IJ}}} W_{n\gamma_{IJ}}. \quad (17)$$

The neutron transmission coefficient  $T_{n_{IJ}}$  comes from the ECIS calculations,

$$T_{n_{IJ}} = 1 - |S_{IJ}|^2, \quad (18)$$

and the transmission coefficients  $T_{\gamma_{IJ}}$  for the radiative capture process are normalized to the  $s$ -wave  $\gamma$ -ray transmission,

$$T_{\gamma_0} = 2\pi \frac{\langle \Gamma_{\gamma_0} \rangle}{D_0}, \quad (19)$$

using the average radiation width (61.3 meV) and mean level spacing (3.24 eV) previously established in this work. Results calculated with the TALYS code are shown in Fig. 16 and compared with the experimental capture cross sections listed in Table III. The theoretical curve times the square root of the incident neutron energy is in the lower side of the experimental trends, but its shape follows the behavior of the  $(n, \gamma)$  cross sections reported by Macklin *et al.* [21]. Such a result could challenge the average radiation width and mean level spacing established in the resonance range. Fortunately, Table VII highlights the existence of two trends in the stellar neutron cross sections of  $^{175}\text{Lu}$  compiled at  $kT = 30$  keV. Our calculations favor the lower value of 1146 mbarns reported by Bao *et al.* [44] and question the higher value of 1219 barns recommended by Mughabghab, which comes from the experimental work of Wisshak *et al.* [20]. Even if a revision of the latest capture data is then recommended for explaining these ambiguous trends, the present work show that reliable neutron cross sections in the keV energy range can be achieved from the use of our average resonance parameters ( $S_0$ ,  $D_0$ , and  $\langle \Gamma_{\gamma_0} \rangle$ ).

TABLE VII. Stellar neutron cross sections of  $^{175}\text{Lu}$  at  $kT = 30$  keV compiled by Beer *et al.*, Bao *et al.*, and Mughabghab and compared to our calculated value.

Library	Year	Ref.	$\sigma_\gamma(E = 30 \text{ keV})$
Beer <i>et al.</i>	1992	[43]	1179(44) mbarns
Bao <i>et al.</i>	2000	[44]	1146(44) mbarns
Mughabghab	2006	[5]	1219(10) mbarns
This work			1125(62) mbarns

## VI. CONCLUSIONS

Results discussed in this paper conclude the study of the neutron induced reactions on the lutetium isotopes started at the Los Alamos National Laboratory using the DANCE array. Performances of the GELINA facility have been used to verify the  $^{175}\text{Lu}$  resonance parameters up to 1 keV, thanks to transmission experiments on natural Lu samples. Present statistical analysis of the resonance parameters shows that more than 10% of  $s$ -wave levels are missed from 250 eV. A mean level spacing lower than 3.5 eV is then expected. The  $s$ -wave neutron cross section ( $\simeq 2.0 \times 10^{-4}$ ) is not corrupted, at least up to 800 eV, as most of the missing levels carry small

reduced neutron width values. For the average radiation width, a value of  $\langle \Gamma_\gamma \rangle = 61.3(59)$  meV is suggested by the total width of 16 resonances below 50 eV. This result agrees with a local systematic value ( $\simeq 60.2$  meV) obtained for the lutetium isotopes from a random combination of several  $\gamma$ -ray strength functions and level density models. As a consequence, the average radiation width of Liou *et al.* (77 meV) is not confirmed by the present study. The total neutron capture cross section at  $kT = 30$  keV calculated with the TALYS code using our  $s$ -wave average parameters is equal to 1125(62) mbarns. This result confirms the value compiled by Bao *et al.* [1146(44) mbarns] which is based on experimental values measured in the 1990s, and questions the higher value of 1219(10) barns recommended by Mughabghab which comes from the more recent experimental work of Wisshak *et al.* reported in 2006. The present  $s$ -wave average resonance parameters could be part of the next update of libraries dedicated to statistical model calculations in order to be challenged by improved theoretical predictions, relying on microscopic calculations.

## ACKNOWLEDGMENTS

The authors wish to express their appreciation for the experimental work performed at the JRC-Geel (Belgium) with the support of the EUFRAT project.

- 
- [1] F. Käppeler, R. Gallino, S. Bisterzo, and W. Aoki, *Rev. Mod. Phys.* **83**, 157 (2011).
- [2] *Handbook for Calculations of Nuclear Reaction Data RIPL*, IAEA-TECDOC-1034 (IAEA, Vienna, 1998).
- [3] T. Belgya *et al.*, *Handbook for Calculations of Nuclear Reaction Data RIPL-2*, IAEA-TECDOC-1506 (IAEA, Vienna, 2006).
- [4] R. Capote *et al.*, *Nucl. Data Sheets* **110**, 3107 (2009).
- [5] S. F. Mughabghab, *Atlas of Neutron Resonances*, 5th ed. (Elsevier, Amsterdam, 2006).
- [6] A. V. Ignatyuk, Summary report of the third research coordination meeting on development of reference input parameter library for nuclear model calculations of nuclear data, International Centre for Theoretical Physics, Trieste, Italy (IAEA, Vienna, Austria, 1997).
- [7] H. I. Liou *et al.*, *Phys. Rev. C* **11**, 1231 (1975).
- [8] O. Roig, *EPJ Web Conf.* **2**, 05003 (2010).
- [9] O. Roig *et al.*, *Nucl. Data Sheets* **119**, 165 (2014).
- [10] D. Denis-Petit, *EPJ Web Conf.* **111**, 02004 (2016).
- [11] D. Denis-Petit, O. Roig, V. Méot, B. Morillon, P. Romain, M. Jandel, T. Kawano, D. J. Vieira, E. M. Bond, T. A. Bredeweg, A. J. Couture, R. C. Haight, A. L. Keksis, R. S. Rundberg, and J. L. Ullmann, *Phys. Rev. C* **94**, 054612 (2016).
- [12] O. Roig *et al.*, *Phys. Rev. C* **93**, 034602 (2016).
- [13] A. Ebran *et al.*, *Phys. Rev. C* **99**, 064603 (2019).
- [14] M. C. Moxon and J. B. Brisland, REFIT computer code, Harwell Laboratory Report No. CBNM/ST/90-131/1, 1990 (unpublished).
- [15] C. W. Reich and M. S. Moore, *Phys. Rev.* **111**, 929 (1958).
- [16] A. M. Lane and R. G. Thomas, *Rev. Mod. Phys.* **30**, 257 (1958).
- [17] H. Henriksson *et al.*, in *Proceedings of the International Conference on Nuclear Data for Science and Technology, Nice, France, 2007*, edited by O. Bersillon *et al.* (EDP Sciences, Les Ulis, France, 2008).
- [18] C. E. Porter and R. G. Thomas, *Phys. Rev.* **104**, 483 (1956).
- [19] A. J. Koning *et al.*, in *Proceedings of the International Conference on Nuclear Data for Science and Technology, Santa Fe, NM, 2004*, edited by R. C. Haight *et al.* (AIP, New York, 2005).
- [20] K. Wisshak, F. Voss, F. Käppeler, and L. Kazakov, *Phys. Rev. C* **73**, 015807 (2006).
- [21] R. L. Macklin *et al.*, Fast neutron capture cross sections of  $^{169}\text{Tm}$ ,  $^{191}\text{Ir}$ ,  $^{193}\text{Ir}$ , and  $^{175}\text{Lu}$  for  $3 < E(n) < 2000$  keV, Los Alamos National Laboratory Report No. LA-7479-MS, 1978 (unpublished).
- [22] H. Beer, G. Walter, R. L. Macklin, and P. J. Patchett, *Phys. Rev. C* **30**, 464 (1984).
- [23] A. Bensussan and J. M. Salome, *Nucl. Instrum. Methods* **155**, 11 (1978).
- [24] L. Salamon *et al.*, *Nucl. Instrum. Methods B* **446**, 19 (2019).
- [25] B. Becker *et al.*, *J. Instrum.* **7**, P11002 (2012).
- [26] W. E. Lamb, *Phys. Rev.* **55**, 190 (1939).
- [27] A. Brusegan *et al.*, *J. Nucl. Sci. Technol.* **39**, 685 (2002).
- [28] A. Santamarina *et al.*, JEFF Report 22, NEA Nuclear Data Services, 2009 (unpublished).
- [29] S. Kopecky *et al.*, in *Proceedings of the International Conference on Nuclear Data for Science and Technology ND2007, Nice, France, 2007*, edited by O. Bersillon *et al.* (EDP Sciences, Les Ulis, France, 2008).
- [30] P. Schillebeeckx *et al.*, in *Neutron Resonance Parameters*, Landolt-Börnstein, New Series, Group I, Volume 26, Part A (Springer-Verlag, Berlin, 2015), Chap. I, section “Neutron resonance spectroscopy for the characterization of materials and objects.”

- [31] C. De Saint Jean *et al.*, *Nucl. Sci. Eng.* **161**, 363 (2009).
- [32] E. Fort and J. P. Doat, ESTIMA computer code, NEA Nuclear Data Committee Report NEANDC-161U, 1983 (unpublished).
- [33] G. Noguere *et al.*, *Nucl. Phys. A* **870–871**, 131 (2011).
- [34] A. Gilbert and A. G. W. Cameron, *Can. J. Phys.* **43**, 1446 (1965).
- [35] S. Goriely and V. Plujko, *Phys. Rev. C* **99**, 014303 (2019).
- [36] E. Rich *et al.*, *Nucl. Sci. Eng.* **162**, 76 (2009).
- [37] G. Noguere, O. Bouland, S. Kopecky, C. Lampoudis, P. Schillebeeckx, A. Plompen, F. Gunsing, C. Sage, and I. Sirakov, *Phys. Rev. C* **92**, 014607 (2015).
- [38] J. Raynal, in *Proceedings of the Specialists' Meeting on the Nucleon Nucleus Optical Model up to 200 MeV, Bruyères-le-Châtel, France, 1996* (Nuclear Energy Agency, Bruyères-le-Châtel, Paris, 1997).
- [39] B. Morillon and P. Romain, *Phys. Rev. C* **74**, 014601 (2006).
- [40] P. Moller *et al.*, *Atomic Data Nucl. Data Tables* **59**, 185 (1995).
- [41] W. Hauser and H. Feshbach, *Phys. Rev.* **87**, 366 (1952).
- [42] P. A. Moldauer, *Phys. Rev. C* **11**, 426 (1978).
- [43] H. Beer *et al.*, *Astrophys. J. Suppl.* **80**, 403 (1992).
- [44] Z. Y. Bao *et al.*, *At. Data Nucl. Data Tables* **76**, 70 (2000).